

FAP106 is an interaction hub for assembling microtubule inner proteins at the cilium inner junction

Received: 28 November 2022

Accepted: 14 July 2023

Published online: 26 August 2023

 Check for updates

Michelle M. Shimogawa¹, Angeline S. Wijono¹, Hui Wang^{1,2,3}, Jiayan Zhang^{1,3,4}, Jihui Sha⁵, Natasha Szombathy¹, Sabeeca Vadakkan¹, Paula Pelayo¹, Keya Jonnalagadda¹, James Wohlschlegel⁵, Z. Hong Zhou^{1,3,4} ✉ & Kent L. Hill^{1,3,4} ✉

Motility of pathogenic protozoa depends on flagella (synonymous with cilia) with axonemes containing nine doublet microtubules (DMTs) and two singlet microtubules. Microtubule inner proteins (MIPs) within DMTs influence axoneme stability and motility and provide lineage-specific adaptations, but individual MIP functions and assembly mechanisms are mostly unknown. Here, we show in the sleeping sickness parasite *Trypanosoma brucei*, that FAP106, a conserved MIP at the DMT inner junction, is required for trypanosome motility and functions as a critical interaction hub, directing assembly of several conserved and lineage-specific MIPs. We use comparative cryogenic electron tomography (cryoET) and quantitative proteomics to identify MIP candidates. Using RNAi knockdown together with fitting of AlphaFold models into cryoET maps, we demonstrate that one of these candidates, MC8, is a trypanosome-specific MIP required for parasite motility. Our work advances understanding of MIP assembly mechanisms and identifies lineage-specific motility proteins that are attractive targets to consider for therapeutic intervention.

Cilia (synonymous with eukaryotic flagella) are conserved, microtubule-based structures that provide motility and signaling functions at the surface of eukaryotic cells. Cilium motility is required for normal human reproduction, development, physiology, and to combat infection¹. Motile cilia also drive cell propulsion in eukaryotic pathogens responsible for tremendous human suffering worldwide^{2,3}. Given this broad distribution and central importance to eukaryote cell biology and human health, understanding structural foundations of cilium assembly and motility is of broad interest.

Most motile cilia are built around a “9 + 2” cylindrical axoneme consisting of nine doublet microtubules (DMTs) surrounding a central pair of singlet microtubules. Each DMT is comprised of a complete, 13-

protofilament A-microtubule (A-tubule) and a partial, 10-protofilament B-microtubule (B-tubule), with non-tubulin proteins forming an “inner junction” (IJ) filament that connects the A- and B-tubules^{4,5}. Recent studies have revealed a previously unappreciated, yet universal feature of motile axonemes, showing that DMTs are not hollow but, instead, are lined with a highly organized network of interconnected “microtubule inner proteins” (MIPs)^{6–9}. Structures inside DMTs had been reported several decades ago in flagellated protozoa^{10,11}, but the diversity and ubiquitous distribution of such structures was not recognized until cryogenic electron tomography (cryoET) enabled high-resolution, 3D structural analysis^{8,12}. Studies in organisms from diverse eukaryotic lineages^{13–17} indicate MIPs are present in both the

¹Department of Microbiology, Immunology and Molecular Genetics, University of California Los Angeles, Los Angeles, CA 90095, USA. ²Department of Bioengineering, University of California Los Angeles, Los Angeles, CA 90095, USA. ³California NanoSystems Institute, University of California Los Angeles, Los Angeles, CA 90095, USA. ⁴Molecular Biology Institute, University of California Los Angeles, Los Angeles, CA 90095, USA. ⁵Department of Biological Chemistry, University of California Los Angeles, Los Angeles, CA 90095, USA. ✉ e-mail: Hong.Zhou@UCLA.edu; kenthill@microbio.ucla.edu

A- and B-tubules and occur in a regularly repeating pattern along the length of the DMT in all motile axonemes. Their broad taxonomic distribution indicates MIPs are fundamentally important for axoneme function and likely were present prior to eukaryote diversification. Meanwhile, absence of regularly spaced MIP structures in non-motile cilia^{18,19} suggests they are required specifically for motile axonemes. Recent work has shown MIPs can influence axoneme stability, structure and beating^{13,15,20–24}. Nonetheless, many aspects of MIP functions and assembly mechanisms remain poorly understood.

In recent, groundbreaking work, cryogenic electron microscopy (cryoEM) was used to reconstruct near-atomic resolution structures of the axoneme, thereby allowing in situ identification and atomic modeling of MIPs in *Chlamydomonas*, *Tetrahymena*, and mammals^{13,15–17,21}. These studies have expanded opportunities for studying MIP function and revealed that while some MIPs are conserved across diverse taxa, others represent lineage-specific adaptations^{13,15–17,21}. Axonemes of diverse organisms share general architecture and beating mechanism, and lineage-specific MIPs therefore offer a potential mechanism for meeting organism-specific motility needs^{2,14,25}, such as those presented by movement of parasitic protozoa through tissues of their human and animal hosts^{26,27}. Identification and analysis of lineage-specific MIPs are therefore of great interest.

African trypanosomes, e.g., *Trypanosoma brucei*, and related kinetoplastids *Trypanosoma cruzi* and *Leishmania* spp., are flagellated, protozoan pathogens that cause extensive human suffering and limit economic development in some of the world's poorest regions^{28,29}. Trypanosomes also represent diverse eukaryotic lineages that have proven useful for uncovering novel features of eukaryote biology^{30,31}. *T. brucei* motility exhibits several distinctive features that support movement through host tissues^{14,32} and is required for pathogenesis³³ and transmission³⁴. The *T. brucei* flagellum has a large and diverse repertoire of MIP structures, including several that are lineage-specific, particularly in the B-tubule¹⁴. Except for a few conserved examples, however, proteins comprising most *T. brucei* MIP structures are unknown, representing a critical knowledge gap in *T. brucei* flagellum assembly and motility.

Here, we investigate MIP function and assembly in *T. brucei* and show that FAPI06 is required for parasite motility and normal flagellum length. Combining cryoET and tandem mass tag (TMT) quantitative proteomics, we further show that *FAP106* knockdown results in loss of conserved IJ MIP structures and their corresponding proteins, as well as several MIP structures and proteins that are lineage-specific. One of these, MC8, is demonstrated by cryoET to be a lineage-specific *T. brucei* MIP and is required for parasite motility. Together, our results demonstrate that FAPI06 is a critical interaction hub required for assembly of conserved and lineage-specific MIPs at the inner junction. This work advances understanding of MIP assembly mechanisms and provides insight into parasite-specific MIPs that are important for *T. brucei* motility. Because they are not present in the mammalian host, such MIPs are attractive for consideration as targets for therapeutic intervention in trypanosome infections.

Results

FAP106 is required for parasite motility

FAP106/Enkur is a conserved B-tubule MIP that forms a “tether loop” structure spanning the inner junction (IJ) and interconnecting several other MIPs^{13,15,21,35}. Enkur is required for motility of mammalian sperm³⁶, but the structural foundation of the motility defect is unknown, and the role of FAP106/Enkur in assembly of the IJ and other MIPs has not been examined. We used tetracycline-inducible RNAi³⁷ to deplete *FAP106* in procyclic form cells, hereafter referred to as “*FAP106* KD”. RNAi knockdown reduced *FAP106* mRNA expression by more than 95% (Fig. 1A) without affecting parasite growth rate (Fig. 1B). *FAP106* KD parasites did not exhibit any gross morphological defects, although their flagella were shorter than normal (Fig. 1C–E). Notably, despite

having a beating flagellum, *FAP106* KD parasites rarely exhibited directional motility, even at high cell densities, which typically result in faster directional motility (Fig. 1F, G and Supplementary Fig. 1). Thus, FAP106 is required, either directly or indirectly, for normal parasite motility.

FAP106 is required for assembly of conserved and lineage-specific MIP structures

To determine whether FAP106 is required for assembly of other MIP structures, we performed cryoET on purified, demembrated flagella from control and *FAP106* KD parasites, processed in parallel. Most known MIPs assemble with a periodicity of 16, or 48 nm^{9,13–15,17,20,21,35,38} and we therefore performed sub-tomogram averaging to determine the 48-nm repeating unit of the DMT (Fig. 2, Supplementary Fig. 2 and Supplementary Movie 1) for comparison to the published structures of the 48-nm repeat from *T. brucei*¹⁴, as well as other organisms^{13,15,21}. The DMT structure in control samples was in good agreement with published structures¹⁴, although we did not clearly resolve the ponticulus, a MIP structure that bisects the B-tubule lumen of mature, but not nascent flagella³⁹, likely due to averaging from the mixture of old and new flagella in the sample.

MIP densities in the A-tubule appeared largely unaffected in the *FAP106* KD relative to the control and, given the position of FAP106 in the B-tubule, we focused our analysis on the B-tubule. Cross-sectional views of the cryoET tomogram show that several major B-tubule MIP densities are missing in the *FAP106* KD (Fig. 2B). Although we do not have sufficient resolution to identify the corresponding proteins directly, we were able to infer the identity of conserved MIPs by referencing their position in other organisms (Supplementary Fig. 3)^{13,15,17,21}. Longitudinal and cross-sectional views show loss of densities corresponding to the “tether loop” structure of FAP106 in algae and mammals^{13,15,21} (Fig. 2B–D, red, Supplementary Movie 1 and Supplementary Fig. 3), consistent with the idea that FAP106 structure is conserved across species¹³. A density corresponding to the expected position of FAP52^{15,21,22} (Supplementary Fig. 3) appears largely unaffected in the *FAP106* KD (Fig. 2B–D, F, tan and Supplementary Movie 1). We did not resolve filamentous densities corresponding to FAP45 on protofilaments B6–B9 in other organisms^{13,15} (Supplementary Fig. 3), but these protofilaments were heavily decorated in *T. brucei* control cells and relatively devoid of MIP densities in *FAP106* KD (Fig. 2D, F and Supplementary Movie 1). Interestingly, the *FAP106* KD also shows loss of FAP106-associated densities that resemble FAP210 in other organisms (Fig. 2B, D, F, green, Supplementary Movie 1 and Supplementary Fig. 3)^{13,15,21,35}, although a clear FAP210 homolog could not be identified in *T. brucei* based on sequence or structure-based homology searches⁴⁰ (Table 1). Overall, our results indicate that FAP106 is critical for assembly of a subset of B-tubule MIP structures in the vicinity of the IJ.

Beyond conserved MIP structures defined in other organisms, we observed additional densities that were reduced in the *FAP106* KD, which correspond to MIP structures that are not present in all organisms. These lineage-specific MIP structures include a protruding density on protofilament B8, “MIP B8”, protruding densities attached to protofilament A12, “MIP A12”, and a protruding density on protofilament B5, “MIP B5” (Fig. 2B–D, F, Supplementary Movie 1 and Supplementary Fig. 3). Thus, FAP106 is required for assembly of universally conserved, as well as lineage-specific MIPs.

FAP106 is required for IJ filament assembly

The IJ filament is a conserved non-tubulin structure that connects protofilaments A1 and B10 in organisms with cilia^{8,19}. The IJ filament is comprised of PACRG and FAP20 subunits that alternate each 4 nm along the axoneme^{4,5}. Interestingly, most organisms have a single hole in the IJ filament every 96 nm, corresponding to one missing PACRG subunit per 96-nm repeating unit^{8,12,38}. *T. brucei* is unusual in having two holes per 96-nm repeating unit¹⁴ (Fig. 2E and Supplementary Fig. 4). The function of the IJ hole is not known, nor is the structural

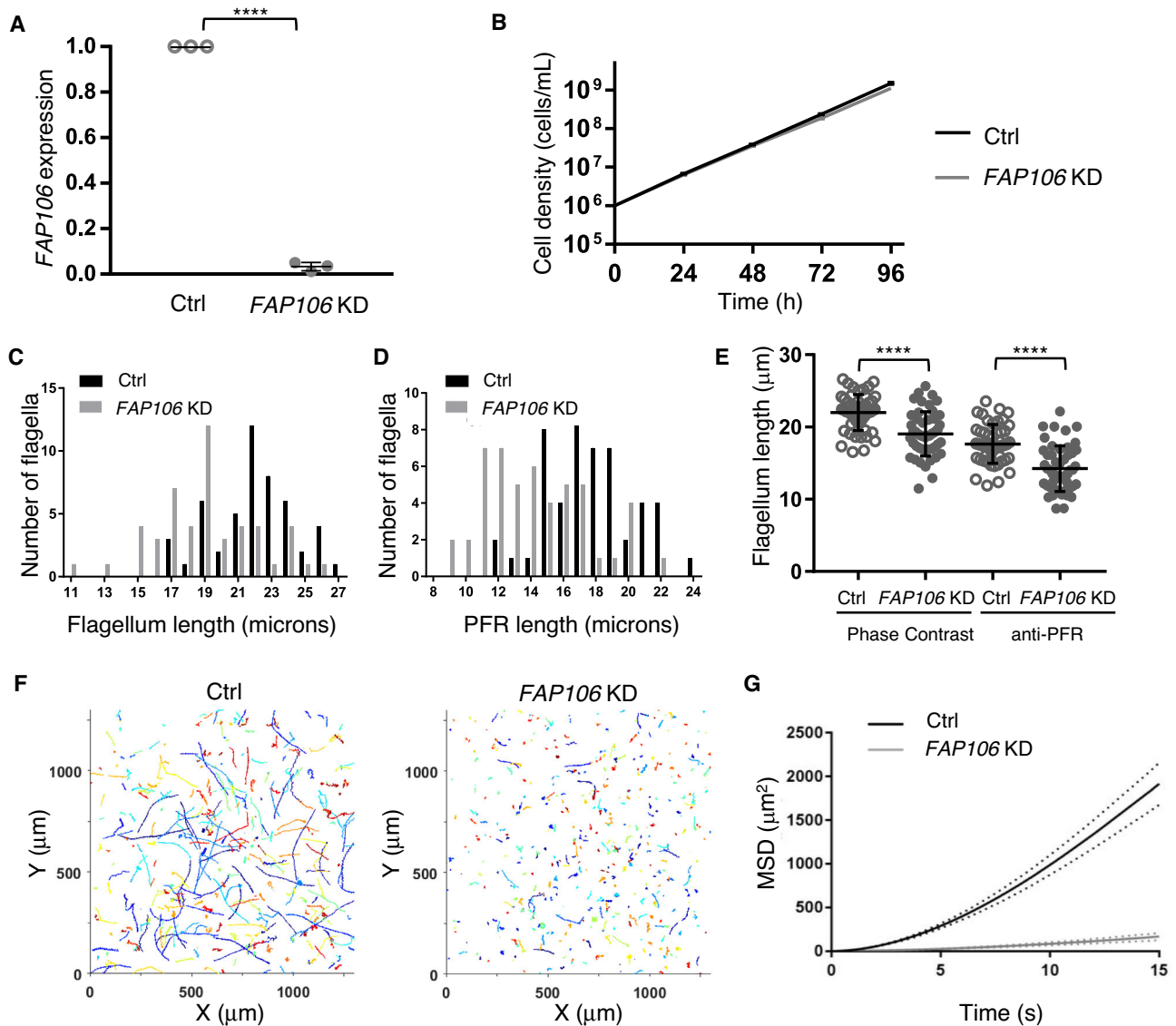


Fig. 1 | *FAP106* is required for parasite motility. 29-13 (Ctrl) and *FAP106* knockdown (*FAP106* KD) parasites were grown in the presence of tetracycline to induce knockdown. **A** qRT-PCR analysis of *FAP106* mRNA levels. Graph shows the mean \pm standard deviation from three independent biological replicates. Unpaired, two-tailed *t*-test **** *p* value ≤ 0.0001 . **B** Cumulative growth curve shows the mean cell density \pm standard deviation vs. time from three independent biological replicates. **C** Histogram shows the length distribution of purified, demembrated flagella. **D** Histogram shows the distribution of paraflagellar rod (PFR) lengths as measured by anti-PFR immunofluorescence microscopy in detergent-extracted

cytoskeletons. **E** Graph shows the mean \pm standard deviation of flagellum lengths in (C) (Phase Contrast) and (D) (anti-PFR). Phase contrast: Ctrl = $22.0 \pm 2.5 \mu\text{m}$, *FAP106* KD = $19.0 \pm 3.1 \mu\text{m}$; anti-PFR: Ctrl = $17.6 \pm 2.7 \mu\text{m}$, *FAP106* KD = $14.2 \pm 3.2 \mu\text{m}$. *N* = 50 flagella for each. Unpaired, two-tailed *t*-test **** *p* < 0.0001. **F** Motility tracks of individual parasites. **G** Mean squared displacement (MSD) of parasites tracked in (F). Dotted lines indicate the upper and lower bounds of the standard error of the mean. Ctrl *N* = 489; *FAP106* KD *N* = 675. Data from an independent biological experiment are shown in Supplementary Fig. 1. Source data are provided as a Source Data file.

basis for the presence of two holes per 96 nm in *T. brucei*. Strikingly, our cryoET data show that loss of *FAP106* results in two additional holes per 48-nm repeat (Fig. 2E), giving six holes per 96-nm repeat (Fig. 2E, Supplementary Fig. 4 and Supplementary Movie 1). These holes correspond to loss of every fourth subunit of the IJ filament (light blue in Fig. 2E), which likely correspond to PACRG, based on analogy with the *Chlamydomonas* structure¹⁵.

TMT proteomics identifies *FAP106*-dependent, lineage-specific MIP proteins

To identify proteins corresponding to *FAP106*-dependent MIP densities, we used tandem mass tag (TMT) quantitative proteomics to compare the protein composition of purified, demembrated flagella from control and *FAP106* KD parasites. We quantified more than 2500

proteins and only eight of these were significantly reduced in flagella from *FAP106* KD parasites (≥ 2 -fold reduced, adjusted *p* value ≤ 0.06) (Fig. 3A, Table 2 and Supplementary Data 1). Three proteins were observed to be increased in the knockdown (Fig. 3A and Supplementary Data 1) and were not studied further.

As expected, the protein most reduced in *FAP106* KD parasites was *FAP106* itself (Fig. 3A and Table 2), confirming efficient knockdown reported by qRT-PCR (Fig. 1A) and loss of *FAP106* protein from the axoneme (Fig. 2). Two other characterized proteins, *FAP45* and PACRG-B, were also reduced in the *FAP106* KD (Fig. 3A, B and Table 2). *FAP45* was almost 4-fold reduced in *FAP106* KD flagella (Fig. 3A and Table 2), supporting results from cryoET that show reduction of densities near the expected location of *FAP45* (Fig. 2, Supplementary Fig. 3 and Supplementary Movie 1) and indicating *FAP106* is required for assembly of

Fig. 2 | FAP106 is required for assembly of conserved and lineage-specific MIP structures. Demembrated flagella were purified from 29-13 (Ctrl) and *FAP106* knockdown (*FAP106* KD) parasites grown in tetracycline to induce knockdown. Structure of the 48-nm repeat of the DMT was obtained by cryoET, with sub-tomographic averaging. Densities are shown as surfaces and colored according to the legend. Conserved MIPs are colored based on similarity to published structures^{13,15,21} (Supplementary Fig. 3). Lineage-specific densities (MIP A12, MIP B5, MIP B8) not present in *Chlamydomonas* or bovine structures are colored to highlight densities that are substantially reduced in *FAP106* KD. **A** Schematic illustrating a cross-section of the “9 + 2” axoneme and paraflagellar rod (PFR) viewed from flagellum tip to base. Adapted from⁷⁵. Enlarged panel shows a single DMT, with A- and B-tubules indicated (A_v, B_v) and protofilaments numbered. FAP106 (red) and the inner junction filament (IJ) comprised of alternating PACRG (blue) and FAP20 (purple) are colored for reference. Viewing angles shown in (C–E) are indicated.

B Cross-sectional view of the DMT. Colored densities indicate structures reduced or missing in *FAP106* KD compared to Ctrl. **C, D** Longitudinal views of the DMT. Viewing angles are indicated in (A), inset. The 48-nm repeat is indicated. Note that *T. brucei* has a structure similar to FAP210 (green) despite not having a clear FAP210 homolog (Table 1). White arrowheads indicate the position of the single hole found within each 48-nm repeat in Ctrl DMTs. **E** Longitudinal views of the DMT, showing the IJ filament. Viewing angles are indicated in (A), inset. The 48-nm repeat is indicated. White arrowheads indicate the position of the single hole found within each 48-nm repeat in Ctrl DMTs. FAP20 and PACRG subunits are colored according to the legend. PACRG-A and PACRG-B are colored to be consistent with TMT proteomics data showing that only PACRG-B is lost in *FAP106* KD (Fig. 3A and Supplementary Data 1), which suggests the extra holes in the *FAP106* KD structure correspond to the position of PACRG-B in control axonemes. **F** Longitudinal view showing reduction of MIP B5 in *FAP106* KD.

position of the extra holes in the *FAP106* KD, specific loss of PACRG-B, and a recent study demonstrating alternating PACRG-A/B homologs in *Tetrahymena*¹⁷, the two IJ holes per 96-nm repeat in control parasites most likely also correspond to missing PACRG-B.

In addition to the known MIPs described above, five previously uncharacterized proteins were reduced in flagella from *FAP106* KD parasites (Fig. 3A and Table 2). One of these proteins (RPC19, Tb927.11.8890) localizes to the nucleus^{43,44}, suggesting it is unlikely to be a MIP. The remaining four proteins (Tb927.10.7120, Tb927.11.4920, Tb927.11.2770, and Tb927.3.3200), are kinetoplastid-specific and localize to the flagellum (Supplementary Fig. 5)^{43,44}, making them strong candidates for lineage-specific, *FAP106*-dependent MIPs. Importantly, these four proteins were separately identified as “MIP candidates”, MC3, MC5, MC8, and MC15, in a completely independent APEX2-based proximity proteomics analysis as being in proximity to B-tubule MIPs FAP45 and FAP52 (detailed in Supplementary Methods; Supplementary Fig. 6 and Supplementary Data 2). APEX2 proximity proteomics identifies proteins in proximity to an APEX2-tagged protein, “the bait”, based

on biotinylation and subsequent streptavidin purification and proteomic identification^{45,46}. Using B-tubule MIPs FAP45 and FAP52 as APEX2-tagged bait, we identified 15 kinetoplastid-specific proteins, which were named MC1-15. Identification of MC3, MC5, MC8, and MC15 as *FAP106*-dependent and adjacent to known B-tubule MIPs greatly supports their assignment as kinetoplastid-specific MIPs.

To test the requirement of MC3, MC5, MC8 and MC15 for flagellum structure and function, we used tetracycline-inducible RNAi to individually knockdown each of these proteins. Knockdown, confirmed by loss of the respective proteins from the flagellum (Supplementary Fig. 5), did not have substantial effects on parasite growth. Loss of MC5 did not affect parasite motility, while MC3, MC8, and MC15 are each required for normal motility (Fig. 3C and Supplementary Fig. 7A). *MC8* KD and *MC15* KD parasites also showed small reductions in flagellum length (Fig. 3D and Supplementary Fig. 7B), while the *MC3* KD did not. To ask whether additional proteins depend on these MCs for assembly into the axoneme, we performed TMT proteomics on flagella isolated from parasites in which the individual MCs were knocked down (Supplementary Fig. 8 and Supplementary Data 1). These proteomic analyses show significant reduction of each MC in the respective knockdown, confirming specific knockdown of the target proteins, but no additional proteins were lost (≥ 2 -fold reduced, adjusted p value ≤ 0.06) in any of the four knockdowns (Supplementary Fig. 8 and Supplementary Data 1). Therefore, motility defects in *MC3*, *MC8*, and *MC15* knockdowns reflect a requirement for these individual, kinetoplastid-specific proteins in trypanosome motility.

MC8 is a lineage-specific *T. brucei* MIP that comprises the MIP B8 density

To discover MIPs corresponding to *FAP106*-dependent MIP densities, we fit the AlphaFold^{47–49} models of the above MCs into our cryoET structures. AlphaFold prediction of individual proteins returned low-confidence predictions for MC3, MC5, and MC15, but predicted that MC8 folds into a structure with a high-confidence pyramid-like domain formed by α helices (Fig. 4A), which fits well into the MIP B8 density (Fig. 4B). To determine whether MC8 in fact corresponds to the MIP B8 density, we performed cryoET on purified, demembrated flagella from control and *MC8* KD parasites, processed in parallel (Fig. 4C–E). In contrast to Fig. 2, both samples resolved a more defined ponticulus structure³⁹ in the B-tubule (Fig. 4C). Importantly, except for this known age-dependent marker³⁹, there are no major differences between the controls from the two experiments, confirming that structures reduced in the *FAP106* KD (Fig. 2) are due to the knockdown and not age-dependent differences. TMT analysis showed that MC8 is the only protein lost in the *MC8* KD (Supplementary Fig. 8C and Supplementary Data 1), so any density altered in the knockdown must correspond to MC8 itself. The sub-tomographic average of the 48-nm repeating unit from *MC8* KD axonemes was nearly identical to that of controls except for the absence of the MIP B8 density (Fig. 4C–E). Thus, MC8 is a bona fide, kinetoplastid-specific B-tubule MIP that is required for normal

Table 1 | Known B-tubule MIPs

<i>Chlamydomonas</i>	Mammals	<i>Tetrahymena</i>	<i>Trypanosoma</i>
^a PACRG	PACRG	PACRGA; PACRGB; PACRGC	Tb927.3.2310; Tb927.9.9940
^a FAP20	CFAP20	CFAP20	Tb927.10.2190
FAP45	CFAP45	CFAP45	Tb927.8.4580
FAP52	CFAP52	CFAP52A; CFAP52B; CFAP52C	Tb927.11.7560
FAP106	ENKUR	CFAP106A; CFAP106B; CFAP106C	Tb927.11.4880
FAP77	CFAP77	CFAP77A; CFAP77B	
FAP210	CFAP210	CFAP210	
FAP90	CFAP90		
FAP126	Flattop		
FAP144	FAM183A		
FAP276	CFAP276		
FAP112		CFAP112A; CFAP112B	
	EFCAB6		
	SPACA9		
		IJ34	
		OJ2	
			Tb927.11.2770 (MIP B8, this study ^b)

^aFAP20 and PACRG form the IJ filament.

^bCorresponding structure was called “MIP3c” in ref. 14 but our current study suggests this structure is distinct from MIP3c (FAP45).

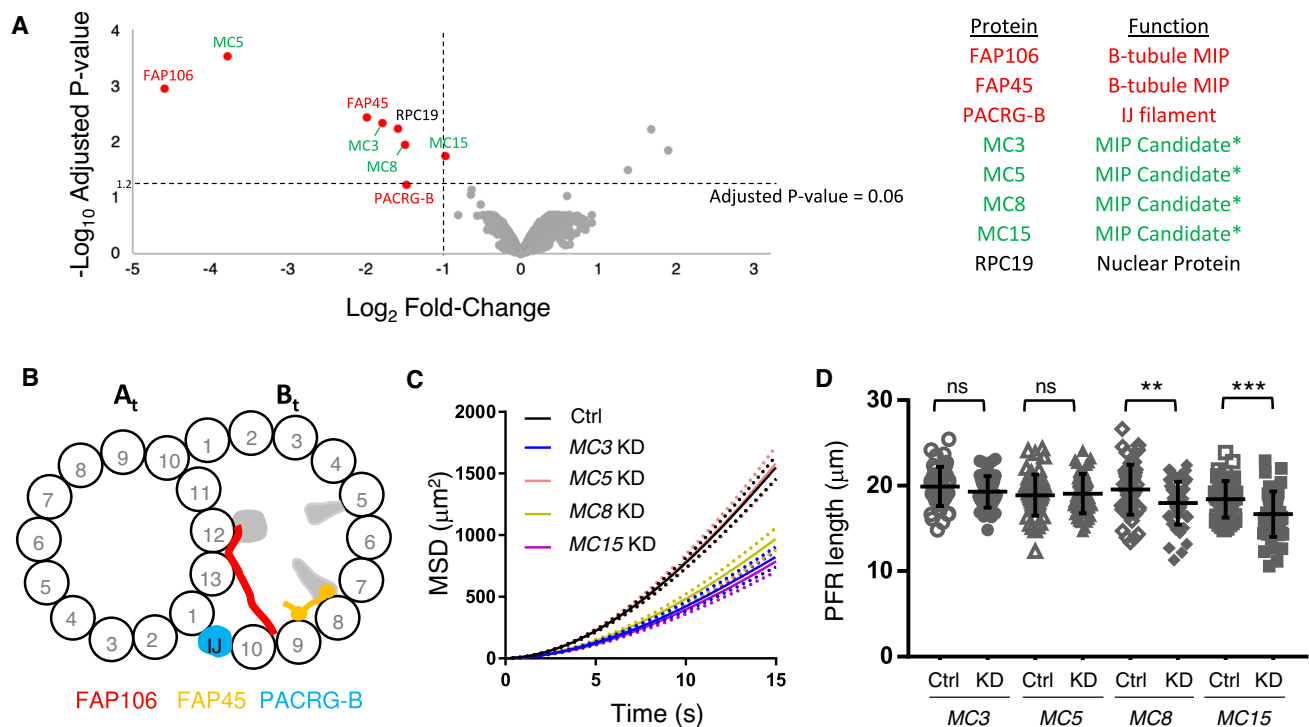


Fig. 3 | TMT proteomics identifies FAP106-dependent, lineage-specific MIP proteins. **A** Demembranated flagella were purified from 29-13 (Ctrl) or *FAP106* KD parasites grown in tetracycline to induce knockdown. Volcano plot shows significance using a moderated two-sided *t*-test with Benjamini–Hochberg adjustment for multiple comparisons ($-\text{Log}_{10}$ Adjusted *p* value) vs. relative abundance in *FAP106* KD/Ctrl (Log_2 Fold-Change) for all proteins quantified by TMT proteomics of two independent biological samples. Proteins meeting the filtering criteria (≥ 2 -fold decrease, adjusted *p* value ≤ 0.06 ; Table 2) are indicated by red dots; text labels indicate known proteins (red) and putative MIP candidates (green). Source data are provided in the Source Data file and Supplementary Data 1. Asterisks indicate proteins independently identified as putative B-tubule MIP candidates in a separate proximity labeling approach (Supplementary Fig. 6 and Supplementary Data 2). **B** Cross-sectional illustration of the DMT as viewed from the flagellum tip, showing the positions of MIP structures lost in *FAP106* KD, with known MIPs

colored and unknown densities in gray, as observed by cryoET (Fig. 2). A- and B-tubules are indicated (A_t , B_t) and protofilaments are numbered. **C** Motility analysis showing mean squared displacement (MSD) of 29-13 (Ctrl) and *MC* KD parasites from ≥ 2 independent biological replicates. Dotted lines indicate the upper and lower bounds of the standard error of the mean. Ctrl *N* = 1761; *MC3* KD *N* = 627; *MC5* KD *N* = 753; *MC8* KD *N* = 709; *MC15* KD *N* = 751. Individual replicates are shown in Supplementary Fig. 7A. **D** Graph shows the mean \pm standard deviation of flagellum lengths as measured by anti-paraflagellar rod (PFR) immunofluorescence microscopy on detergent-extracted cytoskeletons prepared from the indicated KD parasites or their respective mNeonGreen (NG)-tagged parental cell lines (Ctrl). *N* = 50 flagella for each, except *N* = 45 flagella for *MC15*-NG. Unpaired, two-tailed *t*-test: *MC3*-NG vs. *MC3* KD *p* = 0.14, *MC5*-NG vs. *MC5* KD *p* = 0.72, *MC8*-NG vs. *MC8* KD *p* = 0.005 and *MC15*-NG vs. *MC15* KD *p* = 0.0008. Source data and means are provided as a Source Data file.

parasite motility (Fig. 3C and Supplementary Fig. 7A). The motility defect of *MC8* KD parasites, in which the only missing protein is *MC8*, demonstrates importance of lineage-specific MIPs to flagellar motility.

Discussion

FAP106 knockdown provides insights into MIP assembly mechanisms

Functional analysis lags behind identification and structural assignment of MIP proteins. Here we combine functional, structural, and proteomic analysis to demonstrate that the conserved MIP *FAP106* is required for motility and is a key interaction hub for IJ filament and B-tubule MIP structures. The role of *FAP106* as a key interaction hub is emphasized by our finding that, while *FAP106* is required for assembly of *FAP45* and lineage-specific MIP proteins *MC3*, *5*, *8*, and *15* (Figs. 2, 3 and 5), loss of these individual proteins does not affect other MIP proteins or structures (Supplementary Fig. 8, Fig. 4 and Supplementary Data 1²²). Thus, rather than interdependency, our results suggest a hierarchical mechanism for B-tubule MIP assembly. *FAP106*-dependency of *FAP45* and a *FAP210* structural homolog suggests that extensive interactions of *FAP45* and *FAP210* with the tubulin lattice^{13,15} are relatively weak, while interactions with *FAP106*¹³ are critical for stable binding and establishing their periodicity within the 48-nm repeat. This supports the idea that an important role of MIPs is to enable complex assembly of proteins along otherwise uniform

protofilament polymers of tubulin^{13,15,17,20} and suggests that loss of *FAP45* and *FAP210* in *RIB72* mutants⁵⁰ may reflect dependency on *FAP106* rather than a requirement for *RIB72* directly. Our studies also provide a structural explanation for motility defects of *FAP106* mutants in trypanosomes (Fig. 2), and in sperm from *Enkur* mutants in mice³⁶.

The IJ filament subunit PACRG exhibits functional heterogeneity in trypanosomes

PACRG alternates with *FAP20* to form the highly conserved IJ filament^{4,5}. One of the more mysterious features of DMTs is a hole in the IJ filament that occurs once per 96-nm repeat in most organisms and corresponds to a missing *PACRG*^{8,12,38}. *T. brucei* is unusual in having two IJ holes per 96-nm repeat, one at the site of nexin-dynein regulatory complex (NDRC) attachment as observed in other organisms, and one proximal to the NDRC (Supplementary Fig. 4)¹⁴. The proximal hole is devoid of external structures on the DMT (Supplementary Fig. 4)¹⁴, suggesting it is dictated by MIP interactions rather than NDRC attachment, which is proposed for the NDRC hole⁵¹. Our findings support this idea, as loss of *FAP106* results in extra holes in the IJ filament (Fig. 2E and Supplementary Fig. 4). Some organisms have multiple *PACRG* homologs^{17,41,52}. Two *PACRG* homologs in *T. brucei*, *PACRG-A* and *PACRG-B*, have been suggested to be functionally redundant^{41,42}. Our combined structural and proteomics data (Figs. 2E and 3A)

Table 2 | Proteins significantly reduced in *FAP106* KD flagellum skeletons by TMT proteomics

Protein	Gene ID	^a Fold reduction	^b Adjusted p value	Protein localization	Function
FAP106	Tb927.11.4880	24.02	0.0011	Flagellum	B-tubule MIP
FAP45	Tb927.8.4580	3.95	0.0035	Flagellum	B-tubule MIP
PACRG-B	Tb927.9.9940	2.77	0.0576	Flagellum	IJ filament
MC5	Tb927.11.4920	13.74	0.0003	Flagellum	MIP candidate ^c
MC3	Tb927.10.7120	3.44	0.0044	Flagellum	MIP candidate ^c
MC8	Tb927.11.2770	2.81	0.0111	Flagellum	MIP candidate ^c
MC15	Tb927.3.3200	1.95	0.0177	Flagellum	MIP candidate ^c
RPC19	Tb927.11.8890	2.99	0.0055	Nucleus	RNA polymerase

^aSource data are provided as a Source Data file.

^bModerated two-sided t-test with Benjamini–Hochberg adjustment for multiple comparisons.

^cMIP candidates were identified by independent APEX2-based proximity proteomics using known B-tubule MIPs FAP45 and FAP52 as bait (see Supplementary Data 2).

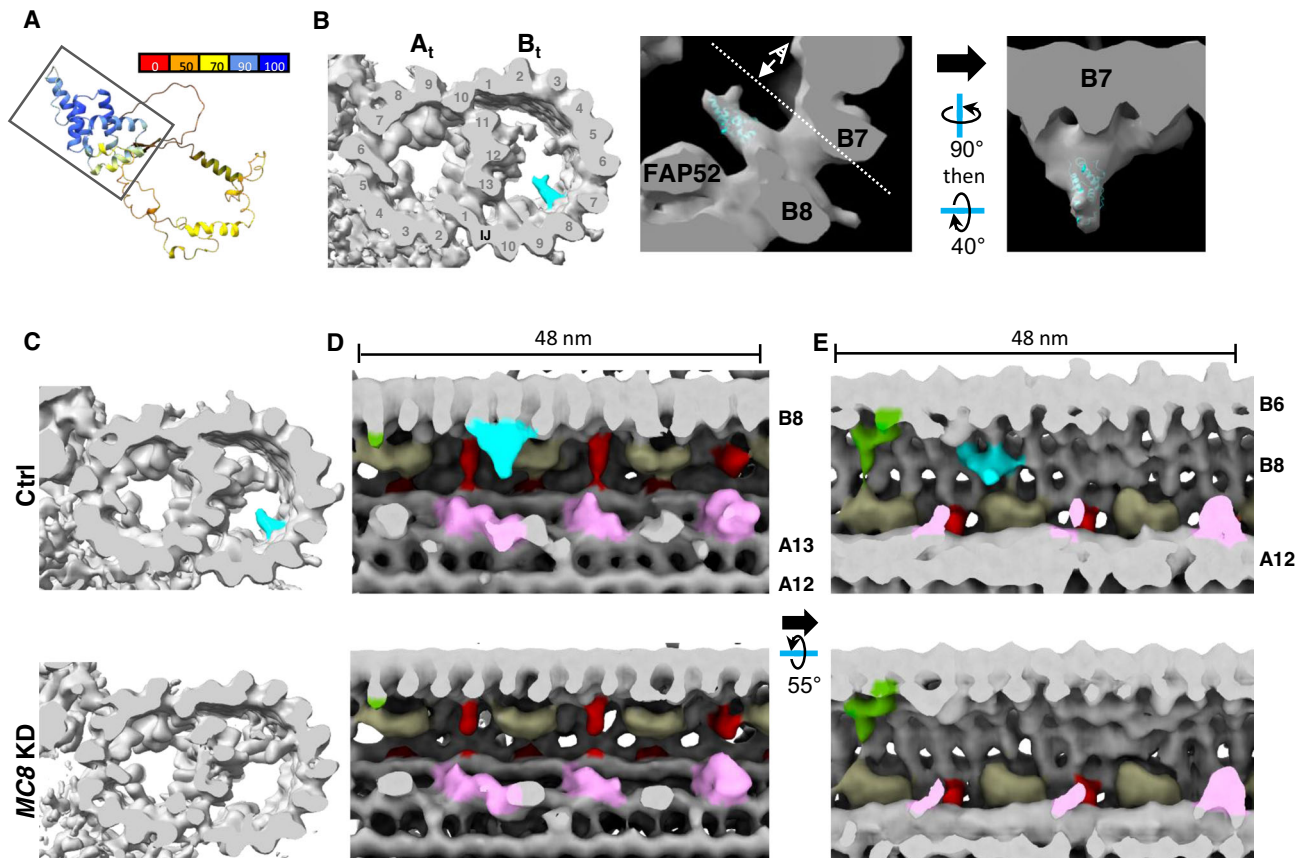


Fig. 4 | MC8 is a lineage-specific *T. brucei* MIP that comprises the MIP B8 density. **A** AlphaFold model for MC8^{47,48}, shown as ribbons and colored according to confidence. Box indicates high-confidence region modeled in **(B)**. **B** MC8 AlphaFold model (ribbon) fitted into MIP B8 cryoET density (gray). **(Left)** Cross-sectional view of the DMT cryoET density map, with the MIP B8 density colored aqua. **(Middle, Right)** Enlarged view of MIP B8 density with AlphaFold model shown in aqua. Viewing angle shown in Right panel is indicated by the dashed line in Middle panel.

C–E Demembrated flagella were purified from 29-13 (Ctrl) and *MC8* knockdown (*MC8* KD) parasites grown in tetracycline to induce knockdown. Structure of the 48-nm repeat of the DMT was obtained by cryoET, followed by sub-tomographic averaging. **C** Cross-sectional view of the DMT with MIP B8 density colored in aqua. **D, E** Longitudinal views of the DMT. Viewing angles and colors are indicated in Fig. 2C, D.

instead support a model in which *T. brucei* PACRG-A and PACRG-B both regularly assemble within each IJ filament, alternating with FAP20 in turn, and with holes in the IJ filament corresponding to missing PACRG-B, but not PACRG-A. Such an arrangement would be consistent with recent data showing alternating PACRG isoforms in *Tetrahymena*¹⁷. Distinct locations and assembly requirements for PACRG-A and PACRG-B indicate they play distinct roles in assembly of the IJ. Although PACRG is conserved among ciliated organisms, the family of PACRG proteins shows substantial heterogeneity in the N-terminal region that has been shown to interact closely with the DMT lattice in *Chlamydomonas*^{17,21,52}. Divergent N-termini of *T. brucei* PACRG-A vs.

PACRG-B may contribute to the differential dependence on FAP106 and their distinct roles in assembly of the IJ.

MC8 is a lineage-specific *T. brucei* MIP that is required for parasite motility

The growing body of evidence suggests IJ subunits (PACRG and FAP20) and a core set of conserved MIPs are found in all motile cilia, while other MIPs vary between organisms^{13–17,21,35,38}. FAP45, FAP52, and FAP106 represent core B-tubule MIPs while FAP126, FAP276, and FAP210 are only found in some organisms (Table 1). MIP A12 densities (Fig. 2B, C, F) are not present in *Chlamydomonas* or mammals^{13,15,21} and

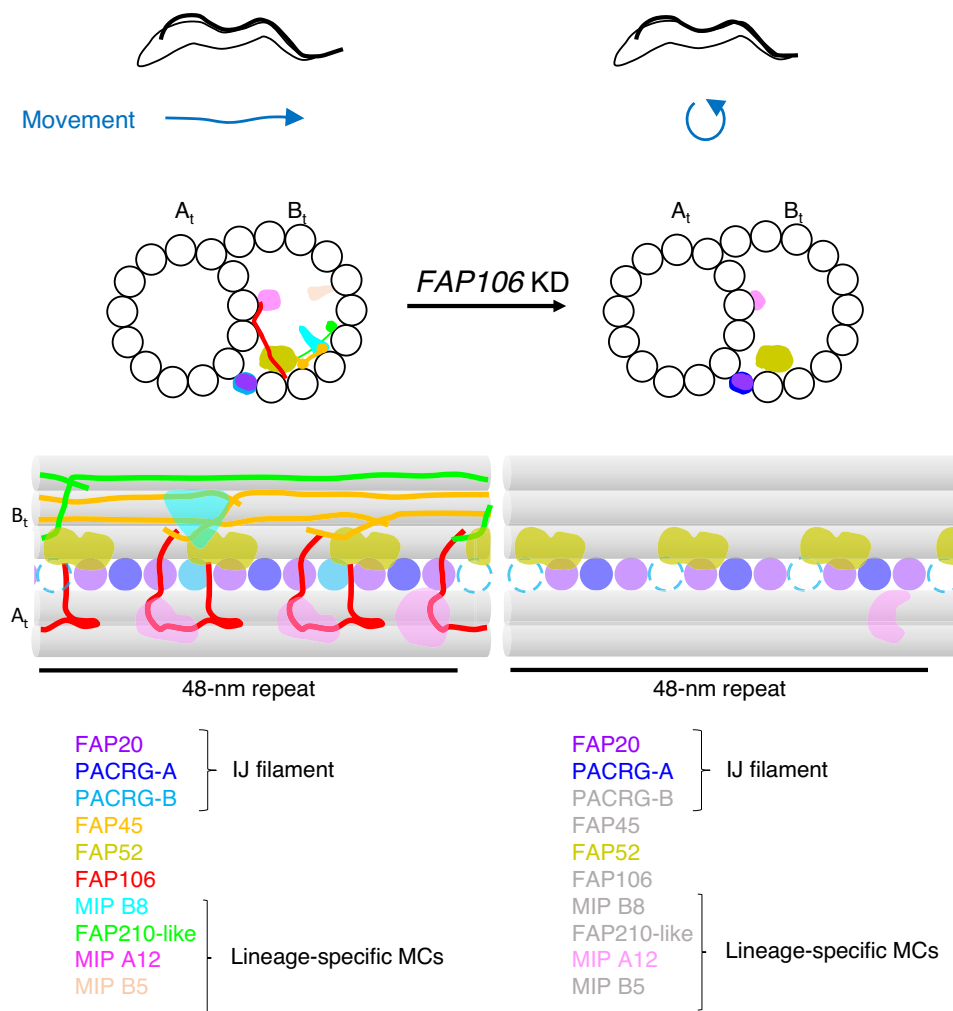


Fig. 5 | FAP106 is required for parasite motility and assembly of conserved and lineage-specific MIPs at the inner junction. Normal parasite motility relies on FAP106 as a critical interaction hub for assembly of MIPs at the inner junction (IJ). Cross-sectional and longitudinal views of the DMT are illustrated. Conserved IJ MIPs PACRG-A, FAP20 and FAP52 assemble independently of FAP106, however PACRG-B

does not stably assemble into the IJ filament without FAP106. The B-tubule remains intact and connected to the A-tubule at the IJ, despite loss of multiple IJ MIPs. FAP106 is also critical for assembly of the conserved MIP, FAP45, and a FAP210-like protein (modeled as filaments based on published structures^{13,15,21}), as well as several previously unknown lineage-specific MIPs.

appear more prominent in *T. brucei* than MIP5a and MIP5b located at a similar position in *Tetrahymena*^{9,17,35,38}, but the proteins that comprise these densities remain unknown. We demonstrate that MC8 is a bona fide lineage-specific MIP corresponding to the MIP B8 structure (Fig. 4). A density with location and periodicity similar to MIP B8 is described in some studies of *Tetrahymena*^{9,17,35,38}, but we were unable to identify any protein outside of kinetoplastids with sequence or structural similarity^{40,47,49} to the MIP B8 protein, MC8. Loss of MC8 in the *FAP106* KD (Fig. 2B–D) is likely due to loss of FAP45, which runs along protofilaments B7–B8^{13,15} and contacts FAP106 directly¹³. Loss of MC8 compromises motility (Fig. 3C and Supplementary Fig. 7A) without affecting other MIPs (Fig. 4 and Supplementary Fig. 8C), demonstrating that lineage-specific MIPs directly impact trypanosome motility. Validation of MC8 as a bona fide *T. brucei* MIP in the current study, through a combination of mutant analysis, structural, functional, and proximity proteomics approaches, demonstrates the power of this combined approach for MIP identification and analysis. Our studies also strongly suggest that MC3, 5, and 15 likewise correspond to lineage-specific *T. brucei* MIPs. Trypanosome motility is necessary for virulence in the mammalian host³³ and transmission through the tsetse fly vector³⁴. Therefore, identification of trypanosome-specific MIPs provides attractive targets to consider for treatment of devastating diseases caused by these pathogens.

Model for assembly of the IJ

Our work provides an important advance toward elucidating the order of MIP assembly and supports the following model for IJ assembly (Fig. 5). FAP20 binds every 8 nm, together with at least a subset of PACRG, to form the IJ filament and this occurs independently from assembly of FAP52²¹ and FAP106 (this work). FAP52 binds every 16 nm, independently of the IJ filament⁴ and FAP106 (this work), and may connect the IJ filament to the B-tubule via FAP276 or other analogous structure^{21,35}. FAP106 also binds every 16 nm, independently from FAP52²¹, bridging the A- and B-tubules directly and serving as a critical guidepost for assembling additional MIPs such as FAP45 and FAP210 (this work). Although FAP52 and FAP106 bind regularly within each 48-nm repeat, their connections to other MIPs differ every 16 nm. Despite apparent contacts between FAP52 and other IJ MIPs^{13,15,21,35}, assembly of IJ MIPs in *Chlamydomonas* is largely unaffected by loss of FAP52²¹. Thus, while FAP52 and FAP106 form contacts with each other and other IJ MIPs, they assemble independently from one another, and FAP106 appears to be more critical for assembly of additional B-tubule MIPs. Going forward, as additional MIPs are identified, particularly those that are lineage-specific, application of combined proteomics, cryoEM, and mutant analysis, as done here, will be necessary to completely define MIP assembly mechanisms and to

yield a full understanding of their contribution to flagellum function.

Methods

Biological materials

All unique biological materials are available from the authors upon request.

Trypanosoma brucei culture

Procyclic *T. brucei brucei* (strain 29-13) originally obtained from George Cross (Rockefeller University)⁵³ were cultivated in SM medium⁵⁴ supplemented with 10% heat-inactivated fetal bovine serum (FBS) at 28 °C with 5% CO₂.

In situ tagging

mNeonGreen and APEX2-tagged cell lines were generated in the 29-13 background by C-terminal tagging⁵⁵ with pPOTv6-puro-puro-mNG or pPOTv7-blast-blast-APEX2-3xHA, respectively. pPOTv7-blast-blast-APEX2-3xHA contains the same APEX2-3xHA tag as in⁴⁶. For MC3-NG, a transient CRISPR-Cas9 system⁵⁶ was used to tag both alleles. See Supplementary Table 2 for list of primers.

Tetracycline-inducible knockdown

Constructs for tetracycline-inducible knockdown were designed using RNAit⁵⁷ and cloned into p2T7-177³⁷. See Supplementary Table 2 for list of primers. NotI-linearized plasmids were transfected into 29-13 (*FAP106* KD) or the corresponding MC-NG tagged cell lines (*MC* KDs) using established methods⁵⁴. Clonal lines were generated by limiting dilution. Knockdown was induced by growing cells in the presence of 1 µg/ml tetracycline (Tet) for at least 3 days. Control parasites were grown in the presence of tetracycline for comparison to the respective KDs. For growth curves, cells were counted with a Beckman Coulter Z1 particle counter and diluted daily to a concentration of 1×10^6 cells/ml, in triplicate.

qRT-PCR

Quantitative real-time PCR (qRT-PCR) was performed as previously described⁵⁸ with the following modifications. *FAP106*-specific primers were designed using RNAit⁵⁷. Analyses were performed in duplicate on three independent RNA preparations and values were normalized to *RPS23*⁵⁹. See Supplementary Table 2 for list of primers.

Motility analyses

Cells were grown to $\sim 1 \times 10^6$ cells/ml and loaded into polyglutamate-coated motility chambers³³ sealed with Vaseline. Thirty second videos were acquired under dark-field illumination at ~ 40 frames per second (fps) using a Hamamatsu ORCA-Flash 4.0 camera on a Zeiss Axio Imager A2 microscope with an EC Plan-Neofluar 10x/0.3 objective lens and Zen 2.6 Pro software. At least five videos were collected for each independent biological replicate. Single cell tracking and mean squared displacement were performed in MATLAB as previously described for fluorescent parasites³³. For “high density” motility analyses, cells were grown to $\sim 1 \times 10^7$ cell/ml, then diluted in conditioned medium to $\sim 1 \times 10^6$ cells/ml and analyzed as above.

Purification of demembrated flagella (detergent-extracted flagellum skeletons)

Detergent extraction was done to demembrate flagellum skeletons, essentially as described¹⁴. Briefly, cells were washed in Dulbecco's PBS (DPBS), resuspended in Extraction buffer (20 mM HEPES, pH 7.4, 1 mM MgCl₂, 150 mM NaCl, 0.5% IGEPAL CA-630 (NP40), 2x Sigmafast EDTA-free protease inhibitor cocktail) for 15 min at room temperature, followed by depolymerization of subpellicular microtubules with 1 mM CaCl₂ on ice for 30 min. Detergent-extracted flagellum skeletons were pelleted at $1500 \times g$ for 10 min at 4 °C.

Flagellum length measurements

For measurements of purified flagella, detergent-extracted flagellum skeletons were prepared as described above and phase contrast images were acquired on a Zeiss Axioskop II microscope with a Plan-Apochromat 63x/1.4 objective lens using Axiovision 4.8 software. For measurements of the paraflagellar rod (PFR) in detergent-extracted cytoskeletons, cells were washed in DPBS and allowed to adhere to glass cover slips for 10 min. Cover slips were rinsed to remove unattached cells, then extracted with PEME buffer (100 mM PIPES, 2 mM EGTA, 1 mM MgSO₄, 0.1 mM EDTA, pH 6.8) + 1% NP40 + 2x Sigmafast EDTA-free protease inhibitor cocktail for 10 min. Cover slips were fixed in methanol at -20 °C for 10 min, allowed to dry, then rehydrated in DPBS for 15 min. Cover slips were blocked in DPBS + 8% normal donkey serum + 2% bovine serum albumin then incubated in rabbit anti-PFR2⁶⁰ primary antibody diluted 1:1000 in blocking solution, followed by donkey anti-rabbit Alexa 594 secondary antibody (Invitrogen A21207) diluted 1:1500 in blocking solution. Cover slips were mounted in Vectashield containing DAPI and images were acquired on a Zeiss Axioskop II fluorescence microscope with a Plan-Apochromat 100x/1.4 objective lens and Axiovision 4.8 software or on a Zeiss Axio Imager Z1 fluorescence microscope with a Plan-Apochromat 63x/1.4 objective lens and Zen software. Flagellum lengths were measured in Fiji using the freehand line tool and analyzed in GraphPad Prism 7.

CryoET

CryoET grids and detergent-extracted flagellum skeletons were prepared essentially as described¹⁴. Briefly, 2×10^8 cells from log phase cultures of similar cell density were harvested and washed twice in DPBS. Flagellum skeletons were prepared as described above, resuspended in 100 µl Extraction buffer and spun over a 30% sucrose cushion in Extraction buffer without NP40 at $800 \times g$ for 5 min at 4 °C. In total, 100–150 µl of flagellum skeletons were collected from the upper fraction, washed once with 700 µl Extraction buffer, and once with 1 ml Extraction buffer without NP40. Flagellum skeletons were resuspended in Extraction buffer without NP40 and vitrified on quantifoil grids with 5 nm fiducial gold beads.

With *SerialEM*⁶¹, tilt series were collected in a Titan Krios instrument equipped with a Gatan imaging filter (GIF) and a post-GIF K3 direct electron detector in electron-counting mode with parameters listed in Supplementary Table 1. Frames in each movie of the raw tilt series were aligned, drift-corrected, and averaged with *Motioncor2*⁶². The micrographs in each tilt series were aligned and reconstructed into 3D tomograms by either weighted back projections (WBP, for subtomographic averaging) or simultaneous iterative reconstruction technique (SIRT, for visualization and particle picking) using the *IMOD* software package⁶³. The contrast transfer function (CTF) was determined by *ctffind4*⁶⁴ and corrected with the *ctfphaseflip* program⁶⁵ of *IMOD*.

As detergent-extracted flagellum skeletons from log-phase cultures contain a mixture of old and new flagella that cannot be distinguished due to lack of cell body remnants, the data represent an unbiased, random sampling of axonemes. Data were collected from the middle region of the flagella to minimize variability due to known differences in protein composition between the proximal and distal ends⁶⁶. To ensure observed differences between samples are due to knockdown of the target protein, rather than age-dependent differences, such as the ponticulus³⁹, comparisons were done only on samples prepared at the same time from cultures maintained at equivalent cell densities and processed identically, in parallel. Validation of this experimental design is provided by sub-tomogram averaging of particles from individual flagella as described in “Sub-tomogram averaging” below.

Sub-tomogram averaging, visualization and modeling

4x binned SIRT reconstructed tomograms were further processed by IsoNet⁶⁷ to improve the contrast for particle picking. Because of their distinct features, radial spokes were picked as particles to represent

the centers of 96-nm axonemal repeat units. These particles of 96-nm repeat units were subject to three rounds of rough alignments with PEET^{7,68}. Major components, such as radial spokes, nexin-dynein regulatory complex and inner junction filament holes, are well resolved in the 96-nm average (Supplementary Fig. 4). To further improve the resolution, particle coordinates for 48-nm repeat units were generated from the coordinates of the aligned particles of 96-nm repeat units. While keeping all coordinates for 96-nm repeat units, extra coordinates for 48-nm repeat units were added unidirectionally from the 96-nm-repeat-units coordinates in a distance of 48 nm along the axonemal axis. PEET alignments were performed on the particles of 48-nm repeat units to generate the final maps. In total, the sub-tomographic averages of flagellar components from four datasets were generated from the following number of particles: 1014 particles from 20 tomograms of Control dataset 1, 1,728 particles from 18 tomograms of *FAP106* KD dataset, 1,936 particles from 52 tomograms of *MC8* KD dataset, and 538 particles from nine tomograms of Control dataset 2. The cryoET sub-tomographic averaged maps have been deposited in the Electron Microscopy Data Bank (EMDB) under the accession codes EMD-28802, EMD-28803, EMD-28804, and EMD-28805, for *FAP106* KD, Control 1, *MC8* KD, and Control 2, respectively. The resolution of each sub-tomographic average was calculated by *calcUnbiasedFSC* in *PEET* based on the 0.143 FSC criterion (Supplementary Fig. 2).

In addition to averaging particles across all tomograms to obtain high-resolution structures, sub-tomographic averages were performed on individual tomograms having more than 50 particles to assess age-dependent structural differences (Supplementary Fig. 9). While of limited resolution, these analyses identified individual flagella with or without a clear ponticulus, which marks mature flagella³⁹, and confirmed that *FAP106*-dependent changes are not a consequence of age-dependent changes (Supplementary Fig. 9).

UCSF ChimeraX⁶⁹ was used to visualize reconstructed tomograms and sub-tomographic averages. For surface rendering with UCSF ChimeraX, maps were first low pass filtered to either 20 Å or 30 Å. Assignment of MIP identities in Figs. 2 and 4 is described in Supplementary Fig. 3. Briefly, the densities corresponding to conserved MIPs were assigned colors based on similarity to published models^{13,15,17,21}. Additional, *FAP106*-dependent lineage-specific densities were colored to highlight changes between the control and knockdown structures. Coloring was done with color zone in ChimeraX, and densities were assigned with colors according to the closest structure in the published atomic model PDB:7rro. Model prediction of *MC8* was performed by AlphaFold Colab^{47–49}. AlphaFold predicted model of *MC8* was superimposed into our averaged density with the *molmap* and *fitmap* functions in UCSF ChimeraX.

TMT labeling and quantitative proteomics

Detergent-extracted flagellum skeletons were prepared from 2×10^8 – 4×10^8 log phase cells as described above. After detergent extraction and depolymerization of subpellicular microtubules, the pellet of flagellum skeletons was washed in Extraction buffer without NP40 and solubilized in 100 μ l 8 M urea, 100 mM Tris, pH 8 for 15 min at room temperature. Samples were centrifuged at 16,000 \times g for 15 min to pellet any insoluble material. The supernatant was diluted with 100 mM Tris, pH 8 to a final concentration of 2 M urea and precipitated with 20% ice-cold trichloroacetic acid (TCA) on ice overnight. The sample was centrifuged at 16,000 \times g for 30 min at 4 °C and washed twice with –20 °C acetone. The TCA-precipitated pellets were dried and stored at ≤ -20 °C.

Sample digestion. Protein pellets were resuspended with digestion buffer (8 M urea, 0.1 M Tris-HCl pH 8.5). Each sample was normalized by absorbance at 280 nm and 25 μ g was aliquoted for the digestion. Samples were reduced and alkylated in digestion buffer via sequential 20-min incubations with 5 mM TCEP and 10 mM iodoacetamide at room

temperature in the dark. Carboxylate-modified magnetic beads (CMMB) also known as SP3⁷⁰ and ethanol (50% final concentration) were added to each sample to induce protein binding to CMMB beads. CMMB beads were washed three times with 80% ethanol and then resuspended with 18 μ l of 100 mM TEAB. Protein samples were digested overnight with 1 μ l of 0.1 μ g/ μ l LysC (Promega) and 2 μ l of 0.4 μ g/ μ l trypsin (Pierce) at 37 °C.

TMT labeling and CIF fractionation. Nine μ l of 100% acetonitrile were added to each sample to a final concentration of 30% (v/v). Then the TMT labels were resuspended with 100% acetonitrile. In total, 25 μ g of each sample was labeled using TMT6plex (Thermo Fisher Scientific) and the four labeled samples of each set (two independent biological replicates each of control and knockdown) were pooled. The pooled samples were fractionated by CMMB-based Isopropanol Gradient Peptide Fractionation (CIF) method⁷¹ into six fractions before mass spectrometry (MS) analysis.

LC-MS acquisition and analysis. Fractionated samples were separated on a 75 μ m ID \times 25 cm C18 column packed with 1.9 μ m C18 particles (Dr. Maisch GmbH) using a 140-min gradient of increasing acetonitrile and eluted directly into a Thermo Orbitrap Fusion Lumos mass spectrometer where MS spectra were acquired using SPS-MS3. Protein identification was performed using MaxQuant⁷² v 1.6.17.0. against a user assembled database consisting of all protein entries from the TriTrypDB (<https://tritypdb.org/tritypdb/app>)⁷³ for *T. brucei* strain 927 (version 7.0). Searches were performed using a 20 ppm precursor ion tolerance. TMT6plex was set as a static modification on lysine and peptide N terminal. Carbamidomethylation of cysteine was set as static modification, while oxidation of methionine residues and N-terminal protein acetylation were set as variable modifications. LysC and Trypsin were selected as enzyme specificity with maximum of two missed cleavages allowed. One percent false discovery rate (FDR) was used as a filter at both protein and PSM levels. Statistical analysis was conducted with the MSstatsTMT Bioconductor package, which uses a moderated *t*-test with Empirical Bayes (variance) moderation of the standard errors and then adjusts the *p* values to account for multiple comparisons by the method of Benjamini–Hochberg FDR⁷⁴.

Reporting summary

Further information on research design is available in the Nature Portfolio Reporting Summary linked to this article.

Data availability

The structure data generated during the current study have been deposited in the Electron Microscopy Data Bank (EMDB) repository, with the accession codes EMD-28802 (*FAP106* KD), EMD-28803 (Control 1), EMD-28804 (*MC8* KD), and EMD-28805 (Control 2). The previously published structure of the DMT from *Bos taurus* shown in Supplementary Fig. 3 is available in the EMDB repository under the accession code EMD-24664 and the atomic model is available as PDB entry 7rro¹³ (<https://doi.org/10.2210/pdb7RRO/pdb>). The raw proteomics data generated during the current study have been deposited to the Mass Spectrometry Interactive Virtual Environment (MassIVE) repository under accession IDs MSV000090661 (<https://doi.org/10.25345/C5M32NF6G>) (TMT proteomics) and MSV000090660 (<https://doi.org/10.25345/C5QV3C80X>) (APEX2 proximity proteomics), and the analysis tables are provided as Supplementary Data 1 and 2, respectively. *T. brucei* genome and protein sequences are publicly available on TriTrypDB⁷³ (<https://tritypdb.org/tritypdb/app>) and protein localizations are publicly available on TrypTag⁴⁴ (<http://tryptag.org>). Source data are provided with this paper.

References

1. Wallmeier, J. et al. Motile ciliopathies. *Nat. Rev. Dis. Primers* **6**, 77 (2020).

2. Kruger, T. & Engstler, M. Flagellar motility in eukaryotic human parasites. *Semin. Cell Dev. Biol.* **46**, 113–127 (2015).
3. Judelson, H. S. & Blanco, F. A. The spores of Phytophthora: weapons of the plant destroyer. *Nat. Rev. Microbiol.* **3**, 47–58 (2005).
4. Dymek, E. E. et al. PACRG and FAP20 form the inner junction of axonemal doublet microtubules and regulate ciliary motility. *Mol. Biol. Cell* **30**, 1805–1816 (2019).
5. Yanagisawa, H. A. et al. FAP20 is an inner junction protein of doublet microtubules essential for both the planar asymmetrical waveform and stability of flagella in Chlamydomonas. *Mol. Biol. Cell* **25**, 1472–1483 (2014).
6. Sui, H. & Downing, K. H. Molecular architecture of axonemal microtubule doublets revealed by cryo-electron tomography. *Nature* **442**, 475–478 (2006).
7. Nicastro, D. et al. The molecular architecture of axonemes revealed by cryoelectron tomography. *Science* **313**, 944–948 (2006).
8. Nicastro, D. et al. Cryo-electron tomography reveals conserved features of doublet microtubules in flagella. *Proc. Natl. Acad. Sci. USA* **108**, E845–E853 (2011).
9. Ichikawa, M. et al. Subnanometre-resolution structure of the doublet microtubule reveals new classes of microtubule-associated proteins. *Nat. Commun.* **8**, 15035 (2017).
10. Anderson, W. A. & Ellis, R. A. Ultrastructure of Trypanosoma Lewisi—flagellum microtubules and kinetoplast. *J. Protozool.* **12**, 483–448 (1965).
11. Vickerman, K. On the surface coat and flagellar adhesion in trypanosomes. *J. Cell Sci.* **5**, 163–193 (1969).
12. Pigino, G. et al. Comparative structural analysis of eukaryotic flagella and cilia from Chlamydomonas, Tetrahymena, and sea urchins. *J. Struct. Biol.* **178**, 199–206 (2012).
13. Gui, M. et al. De novo identification of mammalian ciliary motility proteins using cryo-EM. *Cell* **184**, 5791–5806.e19 (2021).
14. Imhof, S. et al. Cryo electron tomography with volta phase plate reveals novel structural foundations of the 96-nm axonemal repeat in the pathogen. *Elife* **8**, e52058 (2019).
15. Ma, M. et al. Structure of the decorated ciliary doublet microtubule. *Cell* **179**, 909–922.e12 (2019).
16. Gui, M. et al. SPACA9 is a luminal protein of human ciliary singlet and doublet microtubules. *Proc. Natl. Acad. Sci. USA* **119**, e2207605119 (2022).
17. Kubo, S. et al. Native doublet microtubules from Tetrahymena thermophila reveal the importance of outer junction proteins. *Nat. Commun.* **14**, 2168 (2023).
18. Kiesel, P. et al. The molecular structure of mammalian primary cilia revealed by cryo-electron tomography. *Nat. Struct. Mol. Biol.* **27**, 1115–1124 (2020).
19. Sun, S. et al. Three-dimensional architecture of epithelial primary cilia. *Proc. Natl. Acad. Sci. USA* **116**, 9370–9379 (2019).
20. Ichikawa, M. et al. Tubulin lattice in cilia is in a stressed form regulated by microtubule inner proteins. *Proc. Natl. Acad. Sci. USA* **116**, 19930–19938 (2019).
21. Khalifa, A. A. Z. et al. The inner junction complex of the cilia is an interaction hub that involves tubulin post-translational modifications. *Elife* **9**, e52760 (2020).
22. Owa, M. et al. Inner lumen proteins stabilize doublet microtubules in cilia and flagella. *Nat. Commun.* **10**, 1143 (2019).
23. Stoddard, D. et al. Tetrahymena RIB72A and RIB72B are microtubule inner proteins in the ciliary doublet microtubules. *Mol. Biol. Cell* **29**, 2566–2577 (2018).
24. Ide, T. et al. CFAP53 regulates mammalian cilia-type motility patterns through differential localization and recruitment of axonemal dynein components. *PLoS Genet.* **16**, e1009232 (2020).
25. Rossi, M. et al. Kinematics of flagellar swimming in Euglena gracilis: helical trajectories and flagellar shapes. *Proc. Natl. Acad. Sci. USA* **114**, 13085–13090 (2017).
26. Bargul, J. L. et al. Species-specific adaptations of Trypanosome morphology and motility to the mammalian host. *PLoS Pathog.* **12**, e1005448 (2016).
27. Wilson, L. G., Carter, L. M. & Reece, S. E. High-speed holographic microscopy of malaria parasites reveals ambidextrous flagellar waveforms. *Proc. Natl. Acad. Sci. USA* **110**, 18769–18774 (2013).
28. Buscher, P. et al. Human African trypanosomiasis. *Lancet* **390**, 2397–2409 (2017).
29. Kasozi, K. I. et al. Prevalence of hemoprotozoan parasites in small ruminants along a human-livestock-wildlife interface in western Uganda. *Vet. Parasitol. Reg. Stud. Rep.* **17**, 100309 (2019).
30. Vincensini, L., Blisnick, T. & Bastin, P. 1001 model organisms to study cilia and flagella. *Biol. Cell* **103**, 109–130 (2011).
31. Donelson, J. E., Gardner, M. J. & El-Sayed, N. M. More surprises from Kinetoplastida. *Proc. Natl. Acad. Sci. USA* **96**, 2579–2581 (1999).
32. Kruger, T., Schuster, S. & Engstler, M. Beyond blood: African trypanosomes on the move. *Trends Parasitol.* **34**, 1056–1067 (2018).
33. Shimogawa, M. M. et al. Parasite motility is critical for virulence of African trypanosomes. *Sci. Rep.* **8**, 9122 (2018).
34. Rotureau, B. et al. Forward motility is essential for trypanosome infection in the tsetse fly. *Cell Microbiol.* **16**, 425–433 (2014).
35. Li, S. et al. Electron cryo-tomography structure of axonemal doublet microtubule from. *Life Sci. Alliance* **5**, e202101225 (2022).
36. Jungnickel, M. K. et al. The flagellar protein Enkurin is required for mouse sperm motility and for transport through the female reproductive tract. *Biol. Reprod.* **99**, 789–797 (2018).
37. Wickstead, B., Ersfeld, K. & Gull, K. Targeting of a tetracycline-inducible expression system to the transcriptionally silent minichromosomes of Trypanosoma brucei. *Mol. Biochem. Parasitol.* **125**, 211–216 (2002).
38. Song, K. et al. In situ structure determination at nanometer resolution using TYGRESS. *Nat. Methods* **17**, 201–208 (2020).
39. Vaughan, S., Shaw, M. & Gull, K. A post-assembly structural modification to the lumen of flagellar microtubule doublets. *Curr. Biol.* **16**, R449–R450 (2006).
40. van Kempen, M. et al. Fast and accurate protein structure search with Foldseek. *Nat. Biotechnol.* <https://doi.org/10.1038/s41587-023-01773-0> (2023).
41. Dawe, H. R. et al. The Parkin co-regulated gene product, PACRG, is an evolutionarily conserved axonemal protein that functions in outer-doublet microtubule morphogenesis. *J. Cell Sci.* **118**, 5421–5430 (2005).
42. Broadhead, R. et al. Flagellar motility is required for the viability of the bloodstream trypanosome. *Nature* **440**, 224–227 (2006).
43. Dean, S., Sunter, J. D. & Wheeler, R. J. TrypTag.org: a trypanosome genome-wide protein localisation resource. *Trends Parasitol.* **33**, 80–82 (2017).
44. Billington, K. et al. Genome-wide subcellular protein map for the flagellate parasite Trypanosoma brucei. *Nat. Microbiol.* **8**, 533–547 (2023).
45. Hung, V. et al. Spatially resolved proteomic mapping in living cells with the engineered peroxidase APEX2. *Nat. Protoc.* **11**, 456–475 (2016).
46. Vélez-Ramírez, D. E. et al. APEX2 proximity proteomics resolves flagellum subdomains and identifies flagellum tip-specific proteins in Trypanosoma brucei. *mSphere* **6**, e01090-20 (2021).
47. Jumper, J. et al. Highly accurate protein structure prediction with AlphaFold. *Nature* **596**, 583–589 (2021).
48. Mirdita, M. et al. ColabFold: making protein folding accessible to all. *Nat. Methods* **19**, 679–682 (2022).
49. Wheeler, R. J. A resource for improved predictions of Trypanosoma and Leishmania protein three-dimensional structure. *PLoS ONE* **16**, e0259871 (2021).
50. Fabritius, A. S. et al. Proteomic analysis of microtubule inner proteins (MIPs) in Rib72 null. *Mol. Biol. Cell* **32**, br8 (2021).

51. Heuser, T. et al. The dynein regulatory complex is the nexin link and a major regulatory node in cilia and flagella. *J. Cell Biol.* **187**, 921–933 (2009).
52. Khan, N. et al. Crystal structure of human PACRG in complex with MEIG1 reveals roles in axoneme formation and tubulin binding. *Structure* **29**, 572–586.e6 (2021).
53. Wirtz, E. et al. A tightly regulated inducible expression system for conditional gene knock-outs and dominant-negative genetics in *Trypanosoma brucei*. *Mol. Biochem. Parasitol.* **99**, 89–101 (1999).
54. Oberholzer, M. et al. Approaches for functional analysis of flagellar proteins in African trypanosomes. *Methods Cell Biol.* **93**, 21–57 (2009).
55. Dean, S. et al. A toolkit enabling efficient, scalable and reproducible gene tagging in trypanosomatids. *Open Biol.* **5**, 140197 (2015).
56. Shaw, S. et al. A transient CRISPR/Cas9 expression system for genome editing in *Trypanosoma brucei*. *BMC Res. Notes* **13**, 268 (2020).
57. Redmond, S., Vadivelu, J. & Field, M. C. RNAit: an automated web-based tool for the selection of RNAi targets in *Trypanosoma brucei*. *Mol. Biochem. Parasitol.* **128**, 115–118 (2003).
58. Shimogawa, M. M. et al. Cell surface proteomics provides insight into stage-specific remodeling of the host-parasite interface in *Trypanosoma brucei*. *Mol. Cell Proteomics* **14**, 1977–1988 (2015).
59. Lopez, M. A., Saada, E. A. & Hill, K. L. Insect stage-specific adenylate cyclases regulate social motility in african trypanosomes. *Eukaryot. Cell* **14**, 104–112 (2015).
60. Saada, E. A. et al. Insect stage-specific receptor adenylate cyclases are localized to distinct subdomains of the *Trypanosoma brucei* Flagellar membrane. *Eukaryot. Cell* **13**, 1064–1076 (2014).
61. Mastronarde, D. N. Automated electron microscope tomography using robust prediction of specimen movements. *J. Struct. Biol.* **152**, 36–51 (2005).
62. Li, X. et al. Electron counting and beam-induced motion correction enable near-atomic-resolution single-particle cryo-EM. *Nat. Methods* **10**, 584–590 (2013).
63. Kremer, J. R., Mastronarde, D. N. & McIntosh, J. R. Computer visualization of three-dimensional image data using IMOD. *J. Struct. Biol.* **116**, 71–76 (1996).
64. Rohou, A. & Grigorieff, N. CTFFIND4: Fast and accurate defocus estimation from electron micrographs. *J. Struct. Biol.* **192**, 216–221 (2015).
65. Xiong, Q. et al. CTF determination and correction for low dose tomographic tilt series. *J. Struct. Biol.* **168**, 378–387 (2009).
66. Edwards, B. F. L. et al. Direction of flagellum beat propagation is controlled by proximal/distal outer dynein arm asymmetry. *Proc. Natl. Acad. Sci. USA* **115**, E7341–E7350 (2018).
67. Liu, Y. T. et al. Isotropic reconstruction for electron tomography with deep learning. *Nat. Commun.* **13**, 6482 (2022).
68. Heumann, J. M., Hoenger, A. & Mastronarde, D. N. Clustering and variance maps for cryo-electron tomography using wedge-masked differences. *J. Struct. Biol.* **175**, 288–299 (2011).
69. Goddard, T. D. et al. UCSF ChimeraX: meeting modern challenges in visualization and analysis. *Protein Sci.* **27**, 14–25 (2018).
70. Hughes, C. S. et al. Ultrasensitive proteome analysis using paramagnetic bead technology. *Mol. Syst. Biol.* **10**, 757 (2014).
71. Deng, W. et al. Carboxylate-modified magnetic bead (CMMB)-based isopropanol gradient peptide fractionation (CIF) enables rapid and robust off-line peptide mixture fractionation in bottom-up proteomics. *Mol. Cell Proteomics* **20**, 100039 (2021).
72. Cox, J. & Mann, M. MaxQuant enables high peptide identification rates, individualized p.p.b.-range mass accuracies and proteome-wide protein quantification. *Nat. Biotechnol.* **26**, 1367–1372 (2008).
73. Aslett, M. et al. TriTrypDB: a functional genomic resource for the Trypanosomatidae. *Nucleic Acids Res.* **38**, D457–D462 (2010).
74. Huang, T. et al. MSstatsTMT: statistical detection of differentially abundant proteins in experiments with isobaric labeling and multiple mixtures. *Mol. Cell Proteomics* **19**, 1706–1723 (2020).
75. Zhang, J. et al. Structure of the trypanosome paraflagellar rod and insights into non-planar motility of eukaryotic cells. *Cell Discov.* **7**, 51 (2021).

Acknowledgements

We thank Daniel Velez-Ramirez for technical assistance with APEX2 proximity proteomics and Simon Imhof for helpful discussions. We also thank Astra Bryant for assistance with high speed microscopy. Funding was provided by NIH grants AI052348 (K.L.H.), GM071940 (Z.H.Z.), and GM089778 (J.W.). K.J. was supported by the Beckman Scholars Program (Beckman Foundation). We acknowledge the use of resources in the Electron Imaging Center for Nanomachines supported by UCLA and grants from NIH (S10RR23057 and S10OD018111) and NSF (DBI-1338135 and DMR-1548924).

Author contributions

M.M.S., A.S.W., H.W., J.Z., Z.H.Z., and K.L.H. designed research. M.M.S., A.S.W., H.W., J.Z., J.S., N.S., S.V., P.P., and K.J. performed research. M.M.S., A.S.W., H.W., J.Z., J.S., N.S., S.V., P.P., K.J., J.W., Z.H.Z., and K.L.H. analyzed data. M.M.S., A.S.W., H.W., Z.H.Z., and K.L.H. wrote the paper.

Competing interests

The authors declare no competing interests.

Additional information

Supplementary information The online version contains supplementary material available at <https://doi.org/10.1038/s41467-023-40230-z>.

Correspondence and requests for materials should be addressed to Z. Hong Zhou or Kent L. Hill.

Peer review information *Nature Communications* thanks the anonymous reviewers for their contribution to the peer review of this work. A peer review file is available.

Reprints and permissions information is available at <http://www.nature.com/reprints>

Publisher's note Springer Nature remains neutral with regard to jurisdictional claims in published maps and institutional affiliations.

Open Access This article is licensed under a Creative Commons Attribution 4.0 International License, which permits use, sharing, adaptation, distribution and reproduction in any medium or format, as long as you give appropriate credit to the original author(s) and the source, provide a link to the Creative Commons licence, and indicate if changes were made. The images or other third party material in this article are included in the article's Creative Commons licence, unless indicated otherwise in a credit line to the material. If material is not included in the article's Creative Commons licence and your intended use is not permitted by statutory regulation or exceeds the permitted use, you will need to obtain permission directly from the copyright holder. To view a copy of this licence, visit <http://creativecommons.org/licenses/by/4.0/>.

© The Author(s) 2023